

Successive single- q and double- q orders in an anisotropic XY model on the diamond structure: a model for quadrupole ordering in $\text{PrIr}_2\text{Zn}_{20}$

Kaito Sasa¹ and Kazumasa Hattori¹

¹*Department of Physics, Tokyo Metropolitan University, Japan*

(Dated: March 6, 2026)

Quadrupole ordering with the ordering wavevector at the L points in $\text{PrIr}_2\text{Zn}_{20}$ under magnetic fields is analyzed using classical Monte Carlo simulations based on an effective Γ_3 quadrupole model on the diamond structure. We demonstrate that competition between the magnetic field and quadrupole anisotropy leads to a rich phase diagram for magnetic fields applied parallel to [001], which includes switching between a single- q state and a double- q state. We also show that a symmetry-allowed biquadratic intersite interaction, corresponding to a hexadecapole interaction, is crucial for reproducing the weak-field topology observed in experiments.

I. INTRODUCTION

Orbital and multipolar degrees of freedom constitute central themes in strongly correlated electron systems [1]. In transition-metal oxides, orbital degeneracy and superexchange interactions give rise to orbital ordering and intertwined spin-orbital phenomena [2, 3]. From a symmetry-based perspective, orbital order corresponds to the spontaneous ordering of multipole moments transforming according to irreducible representations of the local point group. This viewpoint naturally extends to 5d and f-electron systems [4–6], where strong spin-orbit coupling and crystalline electric fields (CEF) generate higher-rank multipoles as active low-energy degrees of freedom [7].

Pr-based cubic 1–2–20 compounds, $\text{PrT}_2\text{X}_{20}$ ($T = \text{Ti, V, Rh, Ir; X = Al, Zn}$), provide prototypical realizations of such multipolar physics [8]. In many members of this family, the CEF ground state of the Pr^{3+} ion is a non-Kramers doublet, which carries Γ_3 electric quadrupole moments (O_{20}, O_{22}) $\sim \{2z^2 - x^2 - y^2, \sqrt{3}(x^2 - y^2)\}$ under the local point group T_d , as well as a T_{xyz} octupole moment, but no magnetic dipole moment [9]. Because time-reversal symmetry protects the doublet while forbidding magnetic dipole ordering, electric quadrupoles serve as the primary order parameters. Multipolar ordering has been experimentally established in several compounds, including ferroquadrupolar order in $\text{PrTi}_2\text{Al}_{20}$ [10, 11], antiferroquadrupolar order in $\text{PrIr}_2\text{Zn}_{20}$ [12–14], and two-stage quadrupolar–octupolar ordering in $\text{PrV}_2\text{Al}_{20}$ [15–17]. These multipolar ordered states have also been investigated theoretically using mean-field theory [18, 19], Monte Carlo simulations [20–22], impurity models [23], and Landau theory [24].

Beyond static ordering, Γ_3 systems also exhibit strong quadrupolar fluctuations and unconventional metallic behavior. In $\text{PrV}_2\text{Al}_{20}$, non-Fermi-liquid behavior and strange-metal transport have been reported [25–27]. At low temperatures inside the multipolar phase, these compounds exhibit superconductivity [12, 28]. Theoretical studies have proposed two-channel Kondo lattice scenarios to describe the interplay between quadrupole moments and conduction electrons [29, 30], while the de-

tail of the superconductivity has not been understood so far. These developments underscore the importance of understanding multipolar interactions [31].

Among many 1–2–20 compounds, $\text{PrIr}_2\text{Zn}_{20}$ is particularly intriguing. An antiferroquadrupolar transition occurs at $T_Q \simeq 0.11$ K, followed by superconductivity at lower temperatures [12]. Neutron diffraction measurements have identified the ordering wavevector at the L point of the Brillouin zone and found a staggered quadrupolar order with O_{22} components on the diamond lattice [14]. Because the diamond lattice possesses four symmetry-related L points, competition among multiple ordering wavevectors is intrinsic to the system.

A remarkable feature emerges under an applied magnetic field. For $\mathbf{H} \parallel [001]$, specific-heat measurements reveal two successive anomalies within a narrow field window [12, 13]. Field-orientation studies further demonstrate pronounced anisotropy in the phase diagram [32]. Phenomenological Landau analyses have suggested that competition between single- q and double- q states may account for the two-stage transition [33]. However, the microscopic origin and the role of fluctuations remain unclear.

In this work, we address this issue by performing classical Monte Carlo simulations of an effective Γ_3 quadrupole model on the diamond structure [20, 21], concentrating on the symmetry breaking physics with neglecting the T_{xyz} octupole moment and the conduction electrons as a zeroth approximation. We demonstrate successive transitions from a paramagnetic phase to a single- q state and subsequently to a double- q state, construct the magnetic-field–temperature phase diagram, and clarify how higher-order multipolar interactions modify the competition among L-point quadrupole modes.

This paper is organized as follows. In Sec. II, we introduce the effective classical model, formulated as an XY model on the diamond structure with single-ion anisotropy characteristic of Γ_3 quadrupole systems. In Sec. III, we present the Monte Carlo results and analyze detailed multiple- q structure factors. In the latter part of Sec. III, we examine the effects of nearest-neighbor biquadratic interactions. Finally, Sec. IV summarizes the mechanism underlying the phase diagram obtained from

the simulations and compares our results with experimental observations.

II. MODEL

In this paper, we consider an effective model for Γ_3 quadrupole moments on the diamond structure. The two-component Γ_3 quadrupole moment is represented by a planar vector degree of freedom $\mathbf{m}_i = (m_{ix}, m_{iy}) \propto (O_{20}, O_{22})$ at site i with the fixed-length constraint $|\mathbf{m}_i| = 1$. We apply a magnetic field \mathbf{H} within the plane spanned by the $[001]$ and $[110]$ directions. In this geometry, the field–quadrupole coupling takes the form $-hm_{ix}$ with $h \propto |\mathbf{H}|^2$ [18]. In addition, cubic symmetry allows a unique single-ion anisotropy $V_i = -b(m_{ix}^3 - 3m_{ix}m_{iy}^2)$ [18]. Using the parametrization $\mathbf{m}_i = (\cos \theta_i, \sin \theta_i)$, the Hamiltonian is given by

$$\mathcal{H} = \sum_{i,j} \left[J_{ij} \cos \theta_{ij} + K_{ij} \cos^2 \theta_{ij} \right] - \sum_i (h \cos \theta_i + b \cos 3\theta_i), \quad (1)$$

where $\theta_{ij} \equiv \theta_i - \theta_j$, and J_{ij} (K_{ij}) denotes the bilinear (biquadratic) exchange interaction on the ij bond. We include exchange interactions up to the fourth neighbor, $J_{1,2,3,4}$. To stabilize L-point quadrupolar orders at wavevectors $\mathbf{q} = \mathbf{k}_1 = (\pi, \pi, \pi)$, $\mathbf{k}_2 = (-\pi, \pi, \pi)$, $\mathbf{k}_3 = (-\pi, -\pi, \pi)$, and $\mathbf{k}_4 = (\pi, -\pi, \pi)$, a positive J_4 is essential, whereas J_3 does not contribute to their stabilization.

For magnetic Heisenberg models on the diamond structure, various incommensurate orders are known to appear [34, 35], partly due to the geometric frustration inherent in the fcc sublattices of the diamond structure [36–38]. Such incommensurate ordering tendencies can be suppressed by J_4 , i.e., the second-neighbor interaction within each fcc sublattice [36]. Following Ref. [33], we set $J_1 = 1 > 0$ as the unit of energy and take $J_3 = 0$ for simplicity. For the biquadratic interaction, which corresponds to the hexadecapole–hexadecapole coupling between f-electron moments, we retain only the nearest-neighbor term, denoted simply by K . This is because K arises from virtual excitations to higher CEF levels and is therefore expected to be smaller in magnitude.

The Hamiltonian (1) is analyzed by classical Monte Carlo simulations employing the Metropolis algorithm combined with the parallel tempering [39]. We consider a cubic cluster of linear size L with periodic boundary conditions along the x , y , and z directions. The total number of sites is $N = 8L^3$. The primitive unit cell consists of one site at $\mathbf{r} \in A$ (fcc sublattice) and another at $\mathbf{r} + (1/4, 1/4, 1/4) \in B$, where we set the lattice constant to unity. For each temperature T , we thermalize the system for 5×10^4 Monte Carlo steps (MCSs), followed by measurements over approximately 10^6 MCSs. Thermal expectation values of an observable O are evaluated as Monte Carlo averages, denoted by $\langle O \rangle$. We also implement global updates $\theta_i \rightarrow \theta_i \pm 2\pi/3$ and $\theta_i \rightarrow -\theta_i$ for all

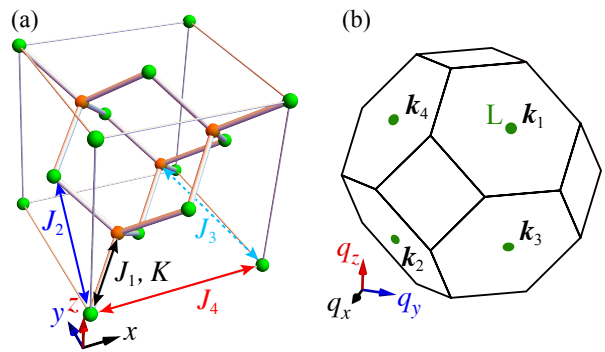


FIG. 1. (a) Diamond structure with the sites for the sublattice A (B) being indicated in green (orange). Exchange interactions $J_{1,2,3,4}$ and K are indicated. (b) The first Brillouin zone. the L points $\mathbf{k}_{1,2,3,4}$ are indicated by green circles.

i . For finite h , only the transformation $\theta_i \rightarrow -\theta_i$ remains a symmetry operation.

III. MONTE CARLO RESULTS

We now present the results of classical Monte Carlo simulations of the Hamiltonian (1). We first consider the case with $K = 0$ and zero magnetic field $h = 0$, and subsequently discuss the effects of a finite magnetic field and the biquadratic interaction.

A. Zero-field thermodynamics

Figure 2(a) shows the temperature dependence of the specific heat C at zero magnetic field ($h = 0$) for $J_2 = K = 0$, $b = 0.5$, and $J_4 = 1$. Two distinct anomalies are clearly visible at $T_1 \simeq 3.010(4)$ and $T_2 \simeq 0.7$, where we have not succeeded in the precise estimation of the error bar for the lower transition temperature T_2 due to large finite size effects. The higher-temperature peak grows with increasing system size, and its position exhibits only weak finite-size dependence, indicating a thermodynamic phase transition. The lower-temperature anomaly is smaller but becomes sharper for larger L , suggesting a second phase transition at T_2 .

To clarify the nature of these transitions, we compute the single- \mathbf{q} structure factor at the L points $\mathbf{q} = \mathbf{k}_\ell$ ($\ell = 1, 2, 3, 4$):

$$S_{\mathbf{k}} \equiv \sum_{\ell=1}^4 \left\langle |\mathbf{m}(\ell)|^2 \right\rangle, \quad (2)$$

$$\mathbf{m}(\ell) = \frac{1}{N} \sum_j p_\ell(j) \mathbf{m}_j e^{i\mathbf{k}_\ell \cdot \mathbf{r}_j}, \quad (3)$$

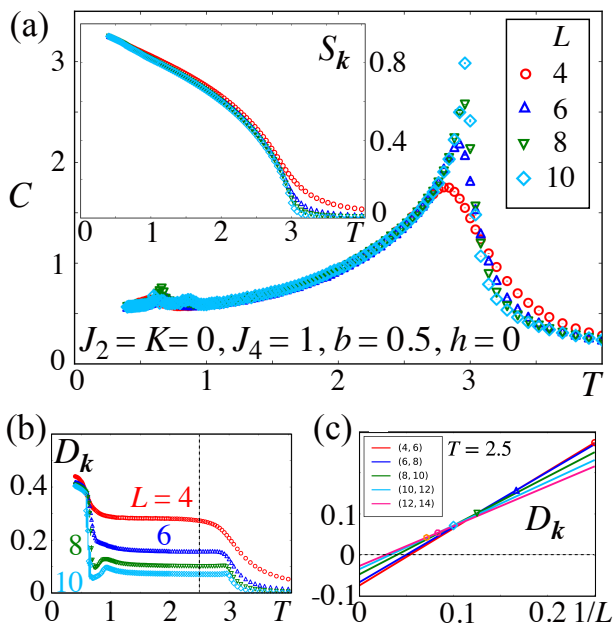


FIG. 2. (a) Specific heat C as a function of T for $(J_2, J_4, K, h) = (0, 1, 0, 0)$ and $L = 4-10$. Inset: single- \mathbf{q} structure factor $S_{\mathbf{k}}$. (b) Double- \mathbf{q} structure factor $D_{\mathbf{k}}$. (c) Extrapolation of $D_{\mathbf{k}}$ to $L \rightarrow \infty$ for $T = 2.5$. See the vertical dashed line in (b). Each straight line is a fit for L and $L + 2$ up to $L = 12$.

where \mathbf{r}_j denotes the position of site j , and

$$p_\ell(j) = \begin{cases} 1, & (\ell = 1), \\ 1, & (\ell \geq 2 \text{ and } j \in A\text{-sublattice}), \\ -1, & (\ell \geq 2 \text{ and } j \in B\text{-sublattice}). \end{cases} \quad (4)$$

We also define the double- \mathbf{q} structure factor as

$$D_{\mathbf{k}} \equiv \sum_{\ell=1}^4 \sum_{\ell' < \ell} \langle |\mathbf{m}(\ell)| |\mathbf{m}(\ell')| \rangle. \quad (5)$$

Note that $D_{\mathbf{k}} \rightarrow 0$ in the thermodynamic limit ($L \rightarrow \infty$) for any single- \mathbf{q} ordered state, whereas $S_{\mathbf{k}}$ remains finite for both single- \mathbf{q} and double- \mathbf{q} orders. Because of the unit-cell convention, \mathbf{k}_1 appears inequivalent in the definition of $p_\ell(j)$ in Eq. (4) compared with the other L points $\mathbf{k}_{2,3,4}$. This apparent asymmetry arises because the direction of \mathbf{k}_1 coincides with the bond direction defining our unit cell. We have numerically confirmed that $\langle |\mathbf{m}(\ell)|^2 \rangle$ is identical for all ℓ within numerical accuracy. This equivalence can also be understood by explicitly constructing the order-parameter configurations for the four cases, which are related to one another by appropriate symmetry operations. See Appendix A for their real-space order parameter configurations.

As shown in the inset of Fig. 2(a), $S_{\mathbf{k}}$ becomes finite for $T < T_1$, exhibiting typical finite-size behavior of a second-order phase transition. Because the Hamiltonian

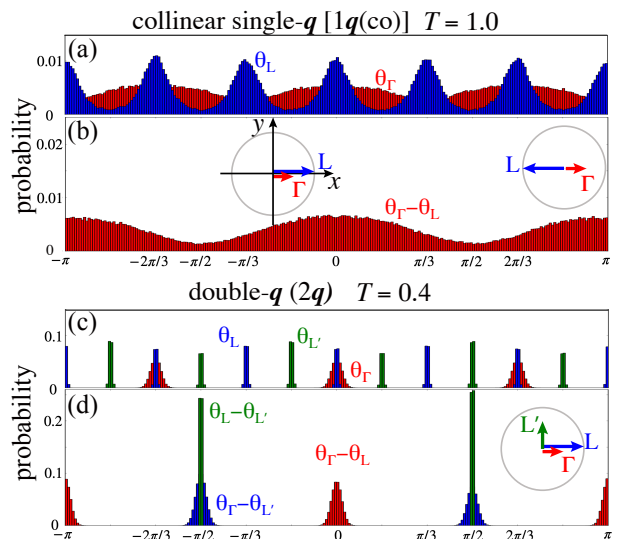


FIG. 3. Order parameter angle distributions for $b = 0.5$, $h = 0$, $J_2 = K = 0$, and $J_4 = 1.0$. The system size is $L = 8$ and 2×10^4 MCSs are used. (a) θ_Γ and θ_L and (b) $\theta_\Gamma - \theta_L$ for $T = 1.0$, where the collinear single- \mathbf{q} order is realized. (c) θ_Γ , θ_L , and $\theta_{L'}$ and (d) $\theta_\Gamma - \theta_L$, $\theta_\Gamma - \theta_{L'}$, $\theta_L - \theta_{L'}$ for $T = 0.4$, where the double- \mathbf{q} order is realized. In the inset in (b) and (d), schematic configurations of order parameters are illustrated for typical selected domains.

(1) possesses threefold rotational symmetry, the transition belongs to the three-dimensional XY universality class, similar to the Néel transition reported in Ref. [20].

To determine whether the ordered state is of single- \mathbf{q} type, we examine $D_{\mathbf{k}}$ [Fig. 2(b)]. For $T < T_2$, the data for $L = 4-10$ saturate to a finite value. We have also inspected Monte Carlo snapshot configurations and find that only two of the $S(\ell)$ components are finite. These results indicate that the low-temperature phase ($T < T_2$) is a double- \mathbf{q} ordered state.

For $T_2 < T < T_1$, the situation is more subtle, as evidenced by the pronounced finite-size effects in Fig. 2(b). To analyze these effects, we extend the system size up to $L = 14$, as shown in Fig. 2(c). Although the accessible sizes are still limited, $D_{\mathbf{k}}$ decreases monotonically toward zero as $1/L \rightarrow 0$. We therefore conclude that a single- \mathbf{q} ordered state is realized in the intermediate-temperature regime $T_2 < T < T_1$. The large finite-size effect might be related to the degeneracy of the single- \mathbf{q} and double- \mathbf{q} orders in the Landau analysis without without mode-mode coupling corrections [33].

Let us discuss the nature of each phase. First, in the single- \mathbf{q} phase, one of the four L-point order parameters $\mathbf{m}(\ell) \equiv \mathbf{m}_L$ becomes finite. Through the single-ion anisotropy V_i , this ordering induces a finite uniform component $\mathbf{m}_\Gamma \equiv N^{-1} \sum_j \mathbf{m}_j$ [18]. Parameterizing

$$\begin{aligned} \mathbf{m}_{L(\Gamma)} &= (m_{L(\Gamma)x}, m_{L(\Gamma)y}) \\ &= |\mathbf{m}_{L(\Gamma)}| (\cos \theta_{L(\Gamma)}, \sin \theta_{L(\Gamma)}), \end{aligned} \quad (6)$$

we analyze the angular distributions of the two modes θ_L and θ_Γ , as shown in Fig. 3(a). Because the data are taken at relatively high temperatures within the ordered phase, the distributions are broad. The peak positions of θ_L occur at $\pi n/3$ (n : integers), while those of θ_Γ appear at 0 and $\pm 2\pi/3$. The distribution of the relative angle $\theta_\Gamma - \theta_L$ is shown in Fig. 3(b), demonstrating that the two components are collinear, i.e., the peaks occur at 0 or π . This configuration corresponds to the collinear single- \mathbf{q} state [$1\mathbf{q}(\text{co})$] obtained for $\mathbf{H} \parallel [001]$ in the Landau analysis of Ref. [33].

Next, in the double- \mathbf{q} phase ($2\mathbf{q}$), an additional L-point order parameter develops. We denote it by $\mathbf{m}(\ell') \equiv \mathbf{m}_{L'} = |\mathbf{m}_{L'}|(\cos \theta_{L'}, \sin \theta_{L'})$, with $|\mathbf{m}_{L'}| \leq |\mathbf{m}_L|$. The corresponding distributions are shown in Figs. 3(c) and 3(d). The peak positions of θ_Γ remain at 0 and $\pm 2\pi/3$, and those of θ_L at $\pi n/3$, as in the single- \mathbf{q} phase. For the secondary L-point component, the preferred orientations are $\theta_{L'} = \pi/2 \pm \pi n/3$. Analysis of the relative-angle distribution reveals that the two symmetry-related L-point components coexist with nearly orthogonal orientations. Such orthogonality minimizes the effective quartic coupling $[\mathbf{m}(\ell) \cdot \mathbf{m}(\ell')]^2$ between modes at \mathbf{q}_ℓ and $\mathbf{q}_{\ell'}$ [33], indicating that fluctuation-induced higher-order terms play a crucial role in stabilizing the double- \mathbf{q} state.

B. Temperature–magnetic-field phase diagram

We next investigate the evolution of the ordered phases under an applied magnetic field. We first consider $\mathbf{H} \parallel [110]$, which corresponds to $h < 0$ in our convention. Neutron scattering experiments on $\text{PrIr}_2\text{Zn}_{20}$ indicate that a single- \mathbf{q} L-point order with $\mathbf{m}(\ell) = (0, m_{Ly})$ is realized for $\mathbf{H} \parallel [\bar{1}10]$. We examine whether our model reproduces this field-induced ordering pattern. We then turn to the case of $\mathbf{H} \parallel [001]$, corresponding to $h > 0$. In the remainder of this subsection, we elucidate the h - T phase diagrams for both field directions and compare the resulting phase structures.

1. $H \parallel [110]$

We consider a magnetic field applied along the $[110]$ direction, corresponding to $h < 0$ in our convention. The pseudo-Zeeman term, $-h \sum_j \cos \theta_j$, explicitly breaks the threefold rotational symmetry of the Hamiltonian (1). This term favors a finite uniform component \mathbf{m}_Γ with $\theta_\Gamma = \pi$.

To distinguish the two components of $\mathbf{m}(\ell) = (m_x(\ell), m_y(\ell))$, we introduce anisotropic structure factors,

$$S_{k_x} \equiv \sum_{\ell=1}^4 \langle |m_x(\ell)|^2 \rangle, \quad S_{k_y} \equiv \sum_{\ell=1}^4 \langle |m_y(\ell)|^2 \rangle. \quad (7)$$

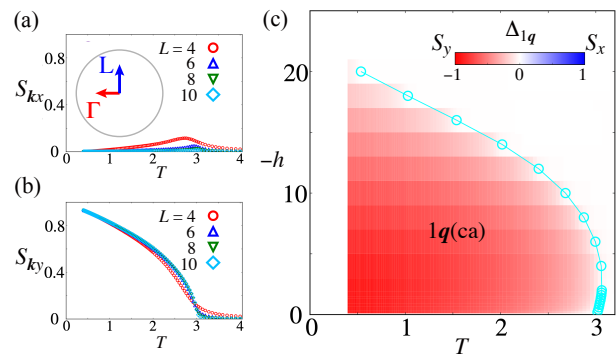


FIG. 4. T dependence of anisotropic structure factor (a) S_{k_x} and (b) S_{k_y} for $h = -1.0$, $b = 0.5$, $J_2 = K = 0$, and $J_4 = 1.0$ with $L = 4, 6, 8$, and 10 . (c) Phase diagram for $\mathbf{H} \parallel [110]$ ($h < 0$). The color map is $\Delta_{1\mathbf{q}} = S_{k_x} - S_{k_y}$ for $L = 8$. The transition temperature for $S_y(\ell)$ is evaluated by the Binder ratio and indicated by circles (cyan). Inset in (a): Schematic order parameter configuration in the canted single- \mathbf{q} phase labeled as $1\mathbf{q}(\text{ca})$.

Figures 4(a) and 4(b) show the temperature dependence of S_{k_x} and S_{k_y} for $h = -1.0$, with the remaining parameters identical to those in Fig. 2. A clear symmetry breaking is observed in the S_{k_y} channel, while there is no signature of double- \mathbf{q} order in $D_{\mathbf{k}}$ (not shown).

The phase diagram for $h < 0$ is presented in Fig. 4(c), where the color scale represents $\Delta_{1\mathbf{q}} \equiv S_{k_x} - S_{k_y}$. A single- \mathbf{q} phase with finite $m_y(\ell)$ and \mathbf{m}_Γ ($\theta_\Gamma = \pi$) is stabilized. In real space, the ordered moments are canted relative to the pseudo-Zeeman field along the x direction in \mathbf{m} space. The robustness of this canted single- \mathbf{q} phase, denoted as $1\mathbf{q}(\text{ca})$ in Fig. 3(c), originates from the cooperative energy gain of the pseudo-Zeeman and single-ion anisotropy terms. The latter can be expressed in Fourier space as $\sim -3b \cos(\theta_\Gamma + 2\theta_L)$, which couples the Γ - and L-point modes [33]. Indeed, one finds $\theta_\Gamma + 2\theta_L = \pi + 2(\pm\pi/2) \equiv 0 \pmod{2\pi}$, so that the single-ion anisotropy energy is minimized consistently with $\theta_\Gamma = \pi$ favored by the pseudo-Zeeman term. For clarity, we do not show results for very small $|h|$, where the double- \mathbf{q} phase persists as in Fig. 2. This indicates that the double- \mathbf{q} state is unstable against small $\mathbf{H} \parallel [110]$ for this parameter set.

2. $H \parallel [001]$

We now discuss the symmetry breaking for $\mathbf{H} \parallel [001]$ ($h > 0$). In this case, the pseudo-Zeeman term induces a uniform moment with $\theta_\Gamma = 0$, opposite in sign to the $\mathbf{H} \parallel [110]$ case discussed in Sec. III B 1. Within a Landau framework, the collinear single- \mathbf{q} configuration incurs a positive quartic term $\sim (\mathbf{m}_\Gamma \cdot \mathbf{m}_L)^2$ in the free energy. Therefore, this state is expected to become unstable at sufficiently large $h > 0$, where a finite $\mathbf{m}_\Gamma = (m_{\Gamma x}, 0)$

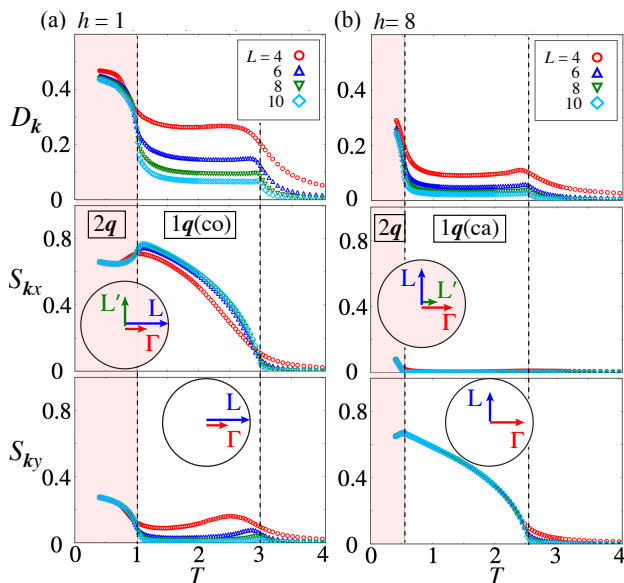


FIG. 5. Double- \mathbf{q} (top), single- \mathbf{q} S_{k_x} (middle), and S_{k_y} (bottom) structure factors for (a) $h = 1$ and (b) $h = 8$, with $L = 4, 6, 8$, and 10 . The other parameters are the same as those in Fig. 4. Vertical dashed line represents the phase boundaries as a guide for eyes. Schematic order parameter configurations are also shown as in Fig. 3.

develops.

Figures 5(a) and 5(b) display $D_{\mathbf{k}}$, S_{k_x} , and S_{k_y} for $h = 1$ and $h = 8$, respectively, with interaction parameters identical to those in Fig. 4. For the lower field $h = 1$ [Fig. 5(a)], two ordered phases appear: the collinear single- \mathbf{q} state [$1\mathbf{q}(\text{co})$] and the double- \mathbf{q} ($2\mathbf{q}$) state, similar to the $h = 0$ case shown in Figs. 2 and 3. As discussed in Sec. III A, the apparent double- \mathbf{q} signal in the intermediate-temperature region $1 \lesssim T \lesssim 3$ is attributed to finite-size effects, as inferred from the L dependence of $D_{\mathbf{k}}$ in the upper panel of Fig. 5(a).

As h increases, the collinear single- \mathbf{q} phase disappears, and the double- \mathbf{q} phase is also suppressed, as shown in Fig. 5(b). This suppression arises because configurations with finite m_{Lx} become energetically unfavorable as the uniform component $m_{\Gamma x}$ grows. Consequently, a canted single- \mathbf{q} phase [$1\mathbf{q}(\text{ca})$] is stabilized, similar to the $h < 0$ case, although the single-ion anisotropy term is not fully minimized when $m_{\Gamma x} > 0$, in contrast to the situation for $h < 0$.

We summarize the T - h phase diagram for $\mathbf{H} \parallel [001]$ in Fig. 6. Because the results for $h \leq 0$ are qualitatively insensitive to microscopic details, we have mainly presented data for the simple parameter set with $J_2 = 0$. Here, we examine the effects of J_2 and b on the phase diagram for $h > 0$.

Figure 6(a) shows the phase diagram for the parameter set used in Figs. 2–5, whereas Fig. 6(b) and Fig. 6(c) correspond to $(J_2, b) = (0.5, 0)$ and $(J_2, b) = (0, 1)$, respectively. In all three cases, the phase diagrams are

qualitatively similar, consisting of three ordered phases: the collinear single- \mathbf{q} phase in the low-field and high-temperature region, the canted single- \mathbf{q} phase in the high-field region, and the double- \mathbf{q} phase in the low-temperature and low-field region. Quantitatively, a positive J_2 suppresses the uniform component, thereby increasing the critical field, as seen in Fig. 6(b) compared with Fig. 6(a). As illustrated by the colormap in Fig. 6, the single-ion anisotropy b tends to align the moments along the x direction in \mathbf{m} space for $h > 0$. Consequently, both the collinear single- \mathbf{q} and the double- \mathbf{q} phases extend to higher fields, as shown in Fig. 6(c).

C. Effect of the biquadratic interaction

We now investigate the effect of the nearest-neighbor biquadratic interaction $K \cos^2 \theta_{ij}$. To clarify how this term modifies the stability of the symmetry-broken phases discussed above, it is convenient to return to the vector representation $\mathbf{m}_i = (m_{xi}, m_{yi})$ and rewrite the interaction in Fourier space:

$$\begin{aligned} \sum_{\langle i,j \rangle} \cos^2 \theta_{ij} &\rightarrow \sum_{\langle i,j \rangle} (\mathbf{m}_i^A \cdot \mathbf{m}_j^B)^2 \\ &= \frac{1}{N} \sum_{\mathbf{p}, \ell, \mathbf{q}} \gamma_{\mathbf{q}} \mathbf{m}_{\mathbf{G}-\mathbf{q}-\mathbf{p}}^A \cdot \mathbf{m}_{\mathbf{q}-\ell}^B \mathbf{m}_{\mathbf{p}}^A \cdot \mathbf{m}_{\ell}^B, \end{aligned} \quad (8)$$

where \mathbf{G} is a reciprocal lattice vector. We take $i \in A$ and $j \in B$ sublattices and denote $\mathbf{m}_i \rightarrow \mathbf{m}_i^A$ and $\mathbf{m}_j \rightarrow \mathbf{m}_j^B$. The structure factor $\gamma_{\mathbf{q}} = \sum_{\delta} e^{i\mathbf{q} \cdot \delta}$ is the nearest-neighbor form factor with $\delta = (0, 0, 0)$, $(-1/2, -1/2, 0)$, $(0, -1/2, -1/2)$, and $(-1/2, 0, -1/2)$. We now extract contributions involving only the L-point order parameters defined in Eq. (3). There are two classes in which all four \mathbf{m} fields belong to L-point modes: (i) $\mathbf{q} = \mathbf{0}$ and (ii) \mathbf{q} at the X points, $\mathbf{q}_X = (2\pi, 0, 0)$, $\mathbf{q}_Y = (0, 2\pi, 0)$, and $\mathbf{q}_Z = (0, 0, 2\pi)$ in Eq. (8). The latter contributions vanish because $\gamma_{\mathbf{q}_X} = \gamma_{\mathbf{q}_Y} = \gamma_{\mathbf{q}_Z} = 0$. Therefore, it suffices to consider the case for $\mathbf{q} = \mathbf{0}$, which yields

$$\gamma_{\mathbf{0}} (\mathbf{m}_{\mathbf{k}_{\ell}}^A \cdot \mathbf{m}_{\mathbf{k}_{\ell'}}^B)^2, \quad (\ell, \ell' = 1, 2, 3, 4), \quad (9)$$

where $\gamma_{\mathbf{0}} = 4$ and we have used $\mathbf{k}_{\ell} \equiv -\mathbf{k}_{\ell}$.

Equation (9) generates corrections to the quartic terms of Landau free energy,

$$\delta f \propto 4K \sum_{\ell=1}^4 \left\{ |\mathbf{m}(\ell)|^4 + \sum_{\ell' < \ell} [\mathbf{m}(\ell) \cdot \mathbf{m}(\ell')]^2 \right\}. \quad (10)$$

For $K > 0$, this contribution favors a double- \mathbf{q} state with mutually orthogonal components $\mathbf{m}(\ell) \perp \mathbf{m}(\ell')$ over a single- \mathbf{q} state near the transition temperature. This can be verified explicitly by substituting, for example, $\{\mathbf{m}(1), \mathbf{m}(2), \mathbf{m}(3), \mathbf{m}(4)\} = \{\mathbf{m}_L, 0, 0, 0\}$ for the single- \mathbf{q} state, and $\frac{1}{\sqrt{2}}\{\mathbf{m}_L, \mathbf{m}_{L'}, 0, 0\}$ with $\mathbf{m}_L \perp \mathbf{m}_{L'}$ and $|\mathbf{m}_L| = |\mathbf{m}_{L'}|$ for the double- \mathbf{q} state. In Landau language, a positive K renormalizes the quartic coefficients

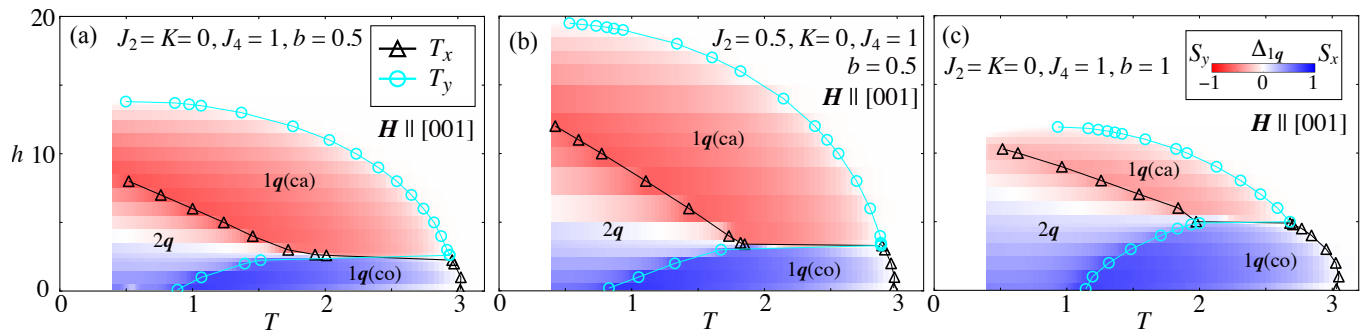


FIG. 6. T - h phase diagrams for $J_4 = 1$, $K = 0$, and $\mathbf{H} \parallel [001]$ ($h > 0$). (a) $(J_2, b) = (0, 0.5)$, (b) $(J_2, b) = (0.5, 0.5)$, and (c) $(J_2, b) = (0, 1)$. The color represents $\Delta_{1\mathbf{q}} = S_{k_x} - S_{k_y}$ for $L = 8$. The symbol indicates the transition temperature T_μ ($\mu = x, y$) at which the S_μ component at the L point orders.

so as to penalize collinear configurations and favor orthogonal mode coupling, driving the system from single- \mathbf{q} to double- \mathbf{q} order.

In accordance with the above analysis, the Monte Carlo results reveal that the biquadratic term $K > 0$ stabilizes the double- \mathbf{q} phase. As K increases, the lower transition temperature T_2 also increases. At $K \simeq 0.4$, T_2 merges with T_1 at $h = 0$. Figures 7(a) and 7(b) show the specific heat C and the double- \mathbf{q} structure factor $D_{\mathbf{k}}$ as functions of T for $h = 0$, respectively. There is only a single anomaly in the T dependence of C , and the system-size dependence of $D_{\mathbf{k}}$ is already small for $L = 10$. Thus, no single- \mathbf{q} state appears for $K = 0.4$.

Figure 7(c) shows the T - h phase diagram for $K = 0.4$ and $\mathbf{H} \parallel [001]$. The double- \mathbf{q} phase indeed expands in the low-field region of the phase diagram. As a result, the collinear phase exists only in the low- h and high- T region. Nevertheless, the collinear phase is stabilized by a small h near the zero-field critical temperature T_1 . The strong stabilization of the double- \mathbf{q} phase due to positive K also leads to an expansion of the double- \mathbf{q} phase for $\mathbf{H} \parallel [110]$, as shown in Fig. 7(d). It should be noted that $\Delta_{1\mathbf{q}} \simeq 0$ (white) in the double- \mathbf{q} phase in both Figs. 7(c) and 7(d). This originates from a cancellation between two modes at the L points with $\mathbf{m}_L \parallel (1, 0)$ and $\mathbf{m}_L \parallel (0, 1)$. This is in stark contrast to the case of $K = 0$ shown in Figs. 6(a)–6(c).

IV. DISCUSSION

In this study, we have analyzed an anisotropic XY model with a cubic single-ion anisotropy characteristic of cubic Γ_3 quadrupole moments. Our focus has been on ordering instabilities at the L points, which are believed to be realized in $\text{PrIr}_2\text{Zn}_{20}$ [14]. Rather than attempting to map out the full phase diagram for general exchange parameters in Eq. (1), we have concentrated on the symmetry-breaking properties when the leading instability occurs at the L points, as motivated by experiments on $\text{PrIr}_2\text{Zn}_{20}$.

Our results clarify that the successive phase transitions arise from competition among symmetry-related L-point components. The double- \mathbf{q} configuration with $\mathbf{m}_L \perp \mathbf{m}_L$ reduces the quartic free-energy cost and is therefore stabilized at low temperatures. This mechanism differs from that proposed for triple- \mathbf{q} quadrupole orders on the fcc lattice [40, 41] and from the mechanism of charge-density-wave ordering in kagome metals [42], where the cubic mode-mode couplings directly couple the modes at the symmetry-related ordering wavevectors. Since our model (1) consists of planer order parameters, the mechanism for the double- \mathbf{q} phases are similar to that discussed in Ref. [43], where magnetic multiple- \mathbf{q} orders are discussed for models with anisotropic bilinear-biquadratic interactions.

The biquadratic interaction further enhances the stability of the double- \mathbf{q} phase, and we have clarified the underlying mechanism. In magnetic Kondo lattice systems, biquadratic interactions are known to stabilize multiple- \mathbf{q} states [44, 45], where higher-order Fermi-surface nesting plays a crucial role. For Pr^{3+} ions with a $4f^2$ configuration whose total angular momentum is $J = 4$, the biquadratic interaction in terms of the Γ_3 pseudospin corresponds to a hexadecapole–hexadecapole coupling and can naturally arise from RKKY processes without invoking higher-order nesting. Indeed, such terms were introduced in the analysis of $\text{PrTi}_2\text{Al}_{20}$ to account for its unusual ferroquadrupolar order under magnetic fields [11]. In the present study, the biquadratic coupling K has been treated phenomenologically; it would be an interesting future direction to derive such higher-order interactions microscopically within the $J = 4$ multiplet framework of f-electron systems [31].

As a comparison with the experimental phase diagram of $\text{PrIr}_2\text{Zn}_{20}$, our results predict that the low-field and low-temperature region is occupied by a double- \mathbf{q} phase. Experimental verification of this prediction would be highly desirable. Upon applying a magnetic field, the double- \mathbf{q} state is destabilized and single- \mathbf{q} orders emerge. For $\mathbf{H} \parallel [001]$, an O_{20} (m_x -type) quadrupole order is stabilized. This phase may correspond to the recently identified but previously unresolved phase reported in Ref. [32].

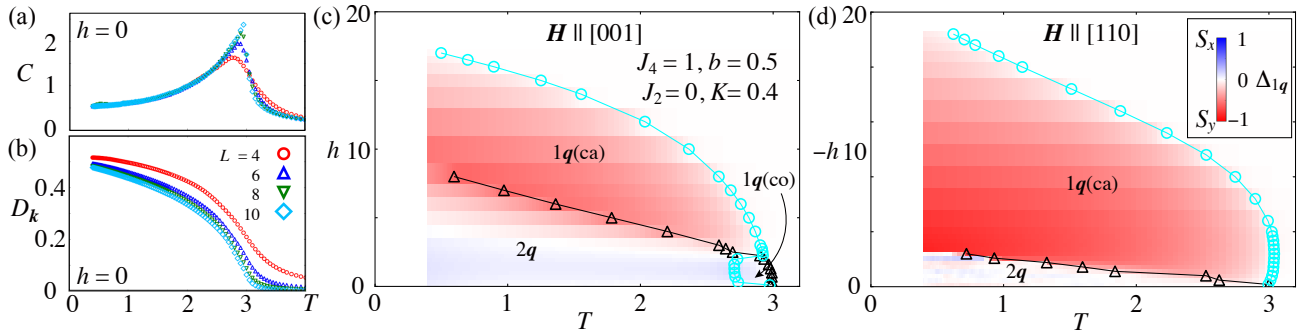


FIG. 7. Temperature dependence of (a) specific heat C and the double- \mathbf{q} structure factor $D_{\mathbf{k}}$ for $K = 0.4$ and $h = 0$. T - h phase diagrams for $J_2 = 0, J_4 = 1, K = 0.4$, and $b = 0.5$: (c) $\mathbf{H} \parallel [001]$ ($h > 0$) and (d) $\mathbf{H} \parallel [110]$ ($h < 0$). The color represents $\Delta_{1\mathbf{q}} = S_{k_x} - S_{k_y}$ for $L = 8$. The symbols in (c) and (d) indicate the transition temperatures similarly to Fig. 6.

Notably, the shape of the phase boundary separating this phase from the low-field phase is reproduced only when a finite biquadratic interaction $K \sim 0.4$ is included. For smaller K , two transitions appear at zero field, inconsistent with experiments [12, 32]. Because this discrepancy persists across several parameter sets with $K = 0$, our results suggest that hexadecapole (biquadratic) interactions play an essential role in $\text{PrIr}_2\text{Zn}_{20}$. In this sense, previous Landau analyses may have overestimated the stability of the double- \mathbf{q} phase due to special corrections arising from integrating out X-point modes.

For $\mathbf{H} \parallel [110]$, an O_{22} (m_y -type) quadrupole order is stabilized, consistent with the neutron scattering results [14]. In specific-heat [12, 32] and thermal-expansion measurements [46], clear signatures of the phase boundaries associated with the low-field double- \mathbf{q} and single- \mathbf{q} phases have not yet been resolved, whereas early ultrasonic experiments reported nearly $|\mathbf{H}|$ -independent anomalies [13].

As for the superconductivity inside the quadrupolar ordered phase [12], it is interesting to note that this superconductivity occurs inside the double- \mathbf{q} phase in our point of view. Although microscopic analysis of this is beyond the scope of this paper, it is highly nontrivial whether the Cooper pairs can be mediated by double- \mathbf{q} quadrupole fluctuations. We leave such analysis in our future problem by extending the discussion in Ref. [47].

Since $\text{PrIr}_2\text{Zn}_{20}$ is currently the only compound for which the multipolar ordering wavevector has been identified, it provides a unique platform for studying correlated multipolar orders in non-Kramers systems. We hope that future experiments will clarify the global phase diagram of $\text{PrIr}_2\text{Zn}_{20}$.

V. SUMMARY

We have demonstrated successive single- \mathbf{q} and double- \mathbf{q} ordering in a quadrupole model using classical Monte Carlo simulations. We have elucidated the T - \mathbf{H} phase diagram, which partially accounts for existing experimen-

tal observations in $\text{PrIr}_2\text{Zn}_{20}$ [12, 13, 32] and provides predictions for yet-unconfirmed phase boundaries by extending the previous Landau analysis [33]. Our results highlight the importance of the biquadratic interaction, corresponding to hexadecapolar coupling, in reproducing the experimentally relevant phase-diagram topology. We hope that this work stimulates further experimental and theoretical studies of multipolar physics in $\text{PrIr}_2\text{Zn}_{20}$ and related compounds.

ACKNOWLEDGMENT

The authors thank T. Onimaru and S. Kittaka for fruitful discussion. This work was supported by JSPS KAKENHI (Grant No. JP23K20824, No. JP23H04866, and No. JP23H04869).

Appendix A: Real space order parameter configurations

We summarize the real-space order parameter configurations for the phases discussed in the main text. Examples of difference in their domain structure as determined by the ordering wavevectors at the L points are also demonstrated.

1. single- \mathbf{q} orders

First, we show the sublattice order parameter configuration for the single- \mathbf{q} phases. Since usual “arrow” representation for the vector XY degrees of freedom might include some misunderstandings for the quadrupole configuration in the real space, we distinguish them by the different color for each sublattice without allows in Fig. 8, where the real-space sublattice configurations are shown for the single- \mathbf{q} phases for (a) $\mathbf{q} = \mathbf{k}_1$ and (b) $\mathbf{q} = \mathbf{k}_2$. The color of spheres indicates the sign of order parameter m_L in $\mathbf{m}_j = (m_\Gamma + m_L, 0)$ or $(m_\Gamma - m_L, 0)$ for the $1q(\text{co})$ and

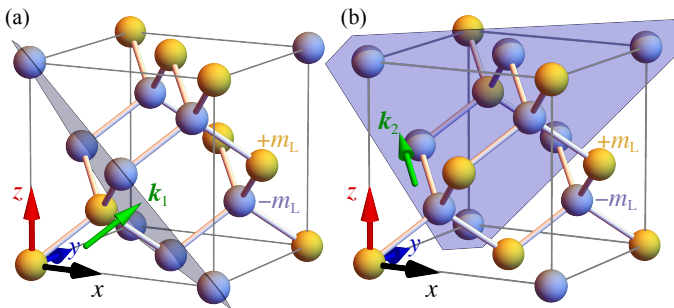


FIG. 8. Real space sublattice patterns for (a) the single- q order with the ordering wavevector (green arrow) $\mathbf{q} = \mathbf{k}_1$ and (b) the single- q order with $\mathbf{q} = \mathbf{k}_2$. Color of spheres represents the order parameter $\pm m_L$. A plane on which the order parameters are uniform is emphasized by a shaded cut.

$\mathbf{m}_j = (m_\Gamma, m_L)$ or $(m_\Gamma, -m_L)$ for the $1q$ (ca), where $m_{\Gamma,L}$ is the ordered moment for the Γ (L) point. Remember the correspondences: $\mathbf{m}_j \propto (1, 0) \leftrightarrow O_{20} \sim 2z^2 - x^2 - y^2$ and $(0, 1) \leftrightarrow O_{22} \sim \sqrt{3}(x^2 - y^2)$.

As represented by the shaded plane perpendicular to \mathbf{k}_n , there are planes where the order parameters are uniform. These planes are arranged along the \mathbf{k}_n direction forming layered structure. For sites with $\pm m_L$, there are three nearest-neighbor sites with $\mp m_L$ and one site with $\pm m_L$. For $\mathbf{q} = \mathbf{k}_1$, the original unit-cell consists of the two sites with m_L (yellow) at the left bottom in Fig 8(a). This corresponds to the factor $p_1(j)$ in Eq. (4). In contrast, for $\mathbf{q} = \mathbf{k}_2$, the two spheres in the original unit-cell are m_L and $-m_L$ in Fig 8(b), reflecting the factor $p_2(j)$ in Eq. (4). As clearly visible in Figs. 8(a) and 8(b), the two domains shown are equivalent after a $\pi/2$ rotation along the z axis and an appropriate translation.

2. double- q orders

Second, the configurations for the double- q phases with $\mathbf{m}_L \perp \mathbf{m}_{L'}$ are shown in Fig. 9, where we use the same convention as in Fig. 8 to illustrate the order parameters. For illustrating the periodicity of the double- q structure, we draw region for eight cubic unit cells and the cubic unit cell is indicated by a thick box in left bottom in each figure. There are four distinct sites with m_L (red), $-m_L$ (blue), $m_{L'}$ (yellow), and $-m_{L'}$ (gray). The real-space order parameter \mathbf{m}_j is given by $\mathbf{m}_j = (m_\Gamma \pm m_L, \pm m_{L'})$ for $\mathbf{m}_L = (m_L, 0)$ and $\mathbf{m}_{L'} = (0, m_{L'})$. Thus, the real-space quadrupole moment is written as

$$\propto O_{20} \cos \eta + O_{22} \sin \eta \text{ with } \tan \eta \equiv \frac{\pm m_{L'}}{m_\Gamma \pm m_L}. \quad (\text{A1})$$

In Fig. 9(a) the two ordering wavevectors are \mathbf{k}_1 and

\mathbf{k}_2 as indicated by the green and orange arrows, respectively. One can notice that each sublattice in the same color form a one-dimensional chain structure along $[0\bar{1}1] \perp \mathbf{k}_1, \mathbf{k}_2$ direction and each site has no nearest-neighbor site with the same color, e.g., a yellow sphere is surrounded by two gray spheres and one red and blue. When the ordering wavevectors are switched to \mathbf{k}_1 and \mathbf{k}_3 as shown in Fig. 9(b), the direction of one-dimensional chains becomes $[\bar{1}10] \perp \mathbf{k}_1, \mathbf{k}_3$. The structure in Fig. 9(b) is identical to that in Fig. 9(a) after C_3 rotation along $[111]$ direction, where $\mathbf{k}_1 \rightarrow \mathbf{k}_1$ and $\mathbf{k}_3 \rightarrow -\mathbf{k}_2 \equiv \mathbf{k}_2$.

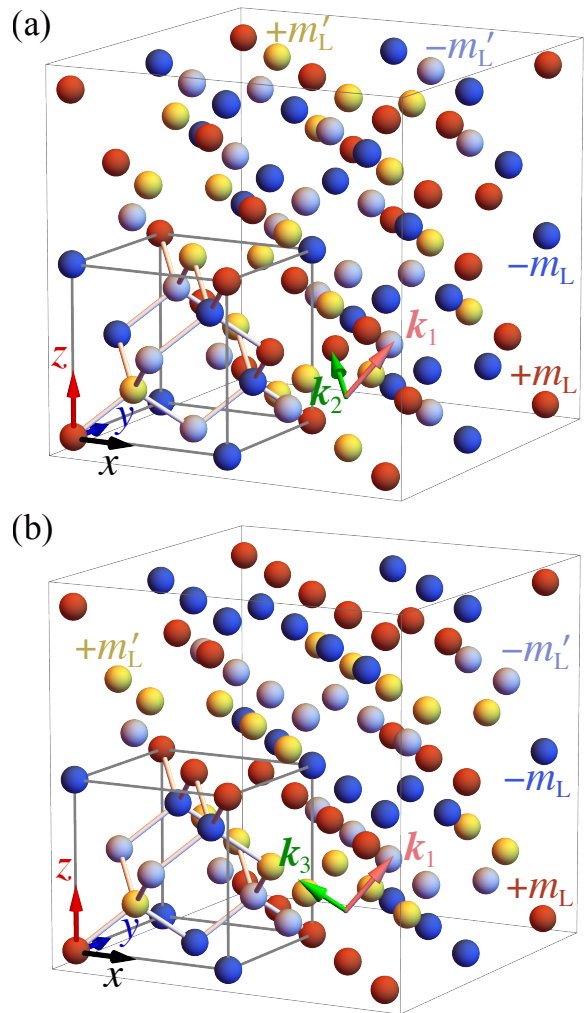


FIG. 9. Real-space sublattice patterns for (a) the double- q order with the ordering wavevectors $\mathbf{q} = \mathbf{k}_1$ (orange arrow) and \mathbf{k}_2 (green arrow) and (b) the double- q order $\mathbf{q} = \mathbf{k}_1$ (orange arrow) and \mathbf{k}_3 (green arrow). Colors represent the sign of the order parameters m_L and $m_{L'}$. The cubic unit cell is shown by a small cubic box.

- [1] Y. Tokura and N. Nagaosa, Orbital physics in transition-metal oxides, *Science* **288**, 462 (2000).
- [2] K. Kugel and D. I. Khomskii, Crystal structure and magnetic properties of substances with orbital degeneracy, *Sov. Phys. JETP* **37**, 725 (1973).
- [3] G. Khaliullin, Orbital order and fluctuations in mott insulators, *Prog. Theor. Phys. Suppl.* **160**, 155 (2005).
- [4] B. J. Kim, H. Jin, S. J. Moon, J.-Y. Kim, B.-G. Park, C. S. Leem, J. Yu, T. W. Noh, C. Kim, S.-J. Oh, J.-H. Park, V. Durairaj, G. Cao, and E. Rotenberg, Novel $J_{\text{eff}} = 1/2$ Mott state induced by relativistic spin-orbit coupling in Sr_2IrO_4 , *Phys. Rev. Lett.* **101**, 076402 (2008).
- [5] G. Jackeli and G. Khaliullin, Mott insulators in the strong spin-orbit coupling limit: from Heisenberg to a quantum compass and Kitaev models, *Phys. Rev. Lett.* **102**, 017205 (2009).
- [6] Y. Kuramoto, H. Kusunose, and A. Kiss, Multipole orders and fluctuations in strongly correlated electron systems, *J. Phys. Soc. Jpn.* **78**, 072001 (2009).
- [7] S. Hayami, M. Yatsushiro, Y. Yanagi, and H. Kusunose, Classification of atomic-scale multipoles under crystallographic point groups and application to linear response tensors, *Phys. Rev. B* **98**, 165110 (2018).
- [8] T. Onimaru and H. Kusunose, Exotic quadrupolar phenomena in non-Kramers doublet systems: The cases of $\text{PrT}_2\text{Zn}_{20}$ ($T = \text{Ir, Rh}$) and $\text{PrT}_2\text{Al}_{20}$ ($T = \text{V, Ti}$), *J. Phys. Soc. Jpn.* **85**, 082002 (2016).
- [9] K. Iwasa, H. Kobayashi, T. Onimaru, K. T. Matsumoto, N. Nagasawa, T. Takabatake, S. Ohira-Kawamura, T. Kikuchi, Y. Inamura, and K. Nakajima, Well-defined crystal field splitting schemes and non-Kramers doublet ground states of f electrons in $\text{PrT}_2\text{Zn}_{20}$ ($T = \text{Ir, Rh, and Ru}$), *J. Phys. Soc. Jpn.* **82**, 043707 (2013).
- [10] S. Kittaka, T. Taniguchi, K. Hattori, S. Nakamura, T. Sakakibara, M. Takigawa, M. Tsujimoto, A. Sakai, Y. Matsumoto, and S. Nakatsuji, Field-orientation effect on ferro-quadrupole order in $\text{PrTi}_2\text{Al}_{20}$, *J. Phys. Soc. Jpn.* **89**, 043701 (2020).
- [11] T. Taniguchi, K. Hattori, M. Yoshida, H. Takeda, S. Nakamura, T. Sakakibara, M. Tsujimoto, A. Sakai, Y. Matsumoto, S. Nakatsuji, and M. Takigawa, Field-induced switching of ferro-quadrupole order parameter in $\text{PrTi}_2\text{Al}_{20}$, *J. Phys. Soc. Jpn.* **88**, 084707 (2019).
- [12] T. Onimaru, K. T. Matsumoto, Y. F. Inoue, K. Umeo, T. Sakakibara, Y. Karaki, M. Kubota, and T. Takabatake, Antiferroquadrupolar ordering in a Pr-based superconductor $\text{PrIr}_2\text{Zn}_{20}$, *Phys. Rev. Lett.* **106**, 177001 (2011).
- [13] I. Ishii, T. Onimaru, K. T. Matsumoto, K. Umeo, T. Sakakibara, and T. Takabatake, Antiferroquadrupolar ordering at the lowest temperatures and magnetic field-temperature phase diagram in the cage compound $\text{PrIr}_2\text{Zn}_{20}$, *J. Phys. Soc. Jpn.* **80**, 093601 (2011).
- [14] K. Iwasa, K. T. Matsumoto, T. Onimaru, T. Takabatake, J.-M. Mignot, and A. Gukasov, Evidence for antiferromagnetic-type ordering of f -electron multipoles in $\text{PrIr}_2\text{Zn}_{20}$, *Phys. Rev. B* **95**, 155106 (2017).
- [15] A. Sakai and S. Nakatsuji, Kondo effects and multipolar order in the cubic $\text{PrTr}_2\text{Al}_{20}$ ($Tr = \text{Ti, V}$), *J. Phys. Soc. Jpn.* **80**, 063701 (2011).
- [16] A. S. Patri, A. Sakai, S. Lee, A. Paramakanti, S. Nakatsuji, and Y. B. Kim, Unveiling hidden multipolar orders with magnetostriction, *Nat. Commun.* **10**, 1 (2019).
- [17] L. Ye, M. E. Sorensen, M. D. Bachmann, and I. R. Fisher, Measurement of the magnetic octupole susceptibility of $\text{PrV}_2\text{Al}_{20}$, *Nat. Commun.* **15**, 7005 (2024).
- [18] K. Hattori and H. Tsunetsugu, Antiferro quadrupole orders in non-Kramers doublet systems, *J. Phys. Soc. Jpn.* **83**, 034709 (2014).
- [19] T. Ishitobi and K. Hattori, Triple- q quadrupole-octupole order scenario for $\text{PrV}_2\text{Al}_{20}$, *Phys. Rev. B* **104**, L241110 (2021).
- [20] K. Hattori and H. Tsunetsugu, Classical Monte Carlo study for antiferro quadrupole orders in a diamond lattice, *J. Phys. Soc. Jpn.* **85**, 094001 (2016).
- [21] F. Freyer, J. Attig, S. Lee, A. Paramakanti, S. Trebst, and Y. B. Kim, Two-stage multipolar ordering in $\text{PrT}_2\text{Al}_{20}$ Kondo materials, *Phys. Rev. B* **97**, 115111 (2018).
- [22] F. Freyer, S. Lee, Y. B. Kim, S. Trebst, and A. Paramakanti, Thermal and field-induced transitions in ferroquadrupolar Kondo systems, *Phys. Rev. Research* **2**, 033176 (2020).
- [23] H. Kusunose, Competing Kondo effects in non-Kramers doublet systems, *J. Phys. Soc. Jpn.* **85**, 064708 (2016).
- [24] S. Lee, S. Trebst, Y. B. Kim, and A. Paramakanti, Landau theory of multipolar orders in $\text{PrY}_2\text{X}_{20}$ kondo materials ($Y = \text{Ti, V, Rh, Ir}$; $X = \text{Al, Zn}$), *Phys. Rev. B* **98**, 134447 (2018).
- [25] Y. Shimura, M. Tsujimoto, B. Zeng, L. Balicas, A. Sakai, and S. Nakatsuji, Field-induced quadrupolar quantum criticality in $\text{PrV}_2\text{Al}_{20}$, *Phys. Rev. B Condens. Matter Mater. Phys.* **91**, 241102(R) (2015).
- [26] A. Wörl, M. Garst, Y. Yamane, S. Bachus, T. Onimaru, and P. Gegenwart, Divergent thermal expansion and Grüneisen ratio in a quadrupolar Kondo metal, *Phys. Rev. Res.* **4**, L022053 (2022).
- [27] M. Lenk, F. Gao, J. Kroha, and A. H. Nevidomskyy, Strange-metal behavior without fine tuning in $\text{PrV}_2\text{Al}_{20}$, *Phys. Rev. Res.* **6**, L042008 (2024).
- [28] K. Matsubayashi, T. Tanaka, A. Sakai, S. Nakatsuji, Y. Kubo, and Y. Uwatoko, Pressure-induced heavy fermion superconductivity in the nonmagnetic quadrupolar system $\text{PrTi}_2\text{Al}_{20}$, *Phys. Rev. Lett.* **109**, 187004 (2012).
- [29] A. Tsuruta and K. Miyake, Non-Fermi liquid and Fermi liquid in two-channel Anderson lattice model: Theory for $\text{PrA}_2\text{Al}_{20}$ ($A = \text{V, Ti}$) and $\text{PrIr}_2\text{Zn}_{20}$, *J. Phys. Soc. Jpn.* **84**, 114714 (2015).
- [30] K. Inui and Y. Motome, Channel-selective non-Fermi liquid behavior in the two-channel Kondo lattice model under a magnetic field, *Phys. Rev. B* **102**, 155126 (2020).
- [31] K. Kubo and T. Hotta, Influence of lattice structure on multipole interactions in Γ_3 non-Kramers doublet systems, *Phys. Rev. B Condens. Matter* **95**, 054425 (2017).
- [32] S. Kittaka, T. Onimaru, K. T. Matsumoto, and T. Sakakibara, Anisotropy of the magnetic-field-induced phase pocket in the non-Kramers doublet system $\text{PrIr}_2\text{Zn}_{20}$, *Phys. Rev. B* **110**, L081106 (2024).
- [33] H. Okanoya and K. Hattori, Orbital orders under magnetic fields in cubic $\text{PrIr}_2\text{Zn}_{20}$, arXiv:2504.10216 10.48550/arXiv.2504.10216 (2025).

- [34] D. Bergman, J. Alicea, E. Gull, S. Trebst, and L. Balents, Order-by-disorder and spiral spin-liquid in frustrated diamond-lattice antiferromagnets, *Nat. Phys.* **3**, 487 (2007).
- [35] S. Lee and L. Balents, Theory of the ordered phase in A-site antiferromagnetic spinels, *Phys. Rev. B* **78**, 144417 (2008).
- [36] C. L. Henley, Ordering by disorder: Ground-state selection in fcc vector antiferromagnets, *J. Appl. Phys.* **61**, 3962 (1987).
- [37] M. Gvozdikova and M. Zhitomirsky, A Monte Carlo study of the first-order transition in a Heisenberg fcc antiferromagnet, *JETP Lett.* **81**, 236 (2005).
- [38] P. Balla, Y. Iqbal, and K. Penc, Degenerate manifolds, helimagnets, and multi-Q chiral phases in the classical Heisenberg antiferromagnet on the face-centered-cubic lattice, *Phys. Rev. Res.* **2**, 043278 (2020).
- [39] K. Hukushima and K. Nemoto, Exchange Monte Carlo method and application to spin glass simulations, *J. Phys. Soc. Jpn.* **65**, 1604 (1996).
- [40] H. Tsunetsugu, T. Ishitobi, and K. Hattori, Quadrupole orders on the fcc lattice, *J. Phys. Soc. Jpn.* **90**, 043701 (2021).
- [41] K. Hattori, T. Ishitobi, and H. Tsunetsugu, Quadrupole partial orders and triple- q states on the face-centered cubic lattice, *Phys. Rev. B* **107**, 205126 (2023).
- [42] M. M. Denner, R. Thomale, and T. Neupert, Analysis of charge order in the kagome metal AV_3Sb_5 $A=K,Rb,Cs$, *Phys. Rev. Lett.* **127**, 217601 (2021).
- [43] S. Hayami, Multiple-Q magnetism by anisotropic bilinear-biquadratic interactions in momentum space, *J. Magn. Magn. Mater.* **513**, 167181 (2020).
- [44] Y. Akagi, M. Udagawa, and Y. Motome, Hidden multiple-spin interactions as an origin of spin scalar chiral order in frustrated Kondo lattice models, *Phys. Rev. Lett.* **108**, 096401 (2012).
- [45] S. Hayami and Y. Motome, Multiple-Q instability by $(d-2)$ -dimensional connections of Fermi surfaces, *Phys. Rev. B* **90**, 060402(R) (2014).
- [46] N. Okamoto, Y. Kono, T. Onimaru, K. T. Matsumoto, K. Hattori, and S. Kittaka, Probing magnetic-field-induced multipolar ordering through field-angle-resolved magnetostriction and thermal expansion in $\text{PrIr}_2\text{Zn}_{20}$, *Phys. Rev. B* **112**, L241113 (2025).
- [47] K. Kubo, Anisotropic superconductivity emerging from the orbital degrees of freedom in a Γ_3 non-Kramers doublet system, *J. Phys. Soc. Jpn.* **87**, 073701 (2018).